




***In vivo* assessment of functional and morphological alterations in tumors under treatment using OCT-angiography combined with OCT-elastography**

MARINA A. SIROTKINA,^{1,*} EKATERINA V. GUBARKOVA,¹ ANTON A. PLEKHANOV,¹  ALEXANDER A. SOVETSKY,² VADIM V. ELAGIN,¹ ALEXANDER L. MATVEYEV,² LEV A. MATVEEV,² SERGEY S. KUZNETSOV,³ ELENA V. ZAGAYNOVA,¹ NATALIA D. GLADKOVA,¹ AND VLADIMIR Y. ZAITSEV²

¹Privolzhsky Research Medical University, Nizhny Novgorod, Russia

²Institute of Applied Physics RAS, Nizhny Novgorod, Russia

³N.A. Semashko Nizhny Novgorod Regional Clinical Hospital, Nizhny Novgorod, Russia

*sirotkina_m@mail.ru

Abstract: Emerging methods of anti-tumor therapies require new approaches to tumor response evaluation, especially enabling label-free diagnostics and *in vivo* utilization. Here, to assess the tumor early reaction and predict its long-term response, for the first time we apply in combination the recently developed OCT extensions - optical coherence angiography (OCA) and compressional optical coherence elastography (OCE), thus enabling complementary functional/microstructural tumor characterization. We study two vascular-targeted therapies of different types, (1) anti-angiogenic chemotherapy (ChT) and (2) photodynamic therapy (PDT), aimed to indirectly kill tumor cells through blood supply injury. Despite different mechanisms of anti-angiogenic action for ChT and PDT, in both cases OCA demonstrated high sensitivity to blood perfusion cessation. The new method of OCE-based morphological segmentation revealed very similar histological structure alterations. The OCE results showed high correlation with conventional histology in evaluating percentages of necrotic and viable tumor zones. Such possibilities make OCE an attractive tool enabling previously inaccessible *in vivo* monitoring of individual tumor response to therapies without taking multiple biopsies.

© 2020 Optical Society of America under the terms of the [OSA Open Access Publishing Agreement](#)

1. Introduction

The Response Evaluation Criteria in Solid Tumors based on tumor size changes (RECIST) still remains the gold standard for tumor response assessment [1]. This approach was developed for evaluation of tumor response to cytotoxic therapies that inhibit cell division [2]. However, the development of new methods of anti-tumor therapies require new ways for tumor response assessment, which could evaluate tumor biology and physiology. In this context, prospects of optical methods attract high interest for tumor response evaluation, including new functional extensions of optical coherence tomography (OCT). The latter are especially convenient for characterization of model tumors in animal experiments, for which the tumor sizes and accessibility perfectly correspond to possibilities of OCT [3–6].

The present study also uses an animal tumor model (murine colon carcinoma) to which two modern types of tumor treatment: anti-angiogenic targeted chemotherapy (ChT) with bevacizumab and photodynamic therapy (PDT) with chlorine E6 photosensitizer - Photodythazin. Both therapies cause tumor vessel damage and, as a result, necrosis of tumor cells through the ischemia.

The mechanism of vasculature-targeted therapy with bevacizumab is as follows. Bevacizumab selectively binds and inhibits the biological activity of vascular endothelial growth factor (VEGF) [7]. As a result, the survival for endothelial cells of pre-existing blood vessels is reduced, a histological picture of desquamation of vascular endothelium, hemostasis and moderate edema are observed [8]. These pathomorphological changes occur after several days and a certain number of ChT sessions. In areas of tumor hypoxia, where blood supply ceased, cell death with the formation of necrosis sites is observed.

PDT is a promising modern approach in cancer therapy with low normal tissue toxicity, widely used in various fields of medicine [9,10]. For vascular-targeted PDT, the photosensitizer (PS) is injected into the bloodstream. Over a short time, the PS is absorbed by endothelial cells. The PS only works after it has been activated by light with certain wavelengths [11]. As a result of the photodynamic reaction, significant changes in endothelial cells occur. This leads to the activation of circulating platelets and other hemostatic mechanisms and, as a consequence, to a thrombogenic effect and blood flow interruption within ~hours post PDT [12]. These processes cause acute hypoxia of the tumor tissue and its death (formation of necrosis).

In view of this, the criteria of tumor response to vascular-targeted therapies should assess not only tumor size changes, but also perfusion and tumor necrosis. For example, in [13] antiangiogenic treatment led to significant decrease in perfusion, mild reduction in mean tumor density without significant change in mean tumor size as demonstrated by computer tomography. In this context, recently developed noninvasive imaging methods open new possibilities to quantitatively assess tumor status and predict treatment response [1].

Among the methods of detection, visualization and quantitative assessment/monitoring of tumor microcirculation (perfusion) OCT-based angiography (OCA) has demonstrated high potential [5,6,14–18]. Recently, observation of blood-circulation blockages in tumors and in peri-tumorous regions based on OCA has proven to be very useful for accurate prediction of the outcome of vasculature-targeted PDT during the first 24 hours post-PDT on experimental animals [5,6] and patients [19], as well as for detection of side effects of radio-therapy manifested via microvasculature alterations in the oral cavity [16]. However, unlike the fairly easily observed perturbation in the microcirculation of blood, the assessment of the histological structure of tissues lacks precise, non-invasive methods.

Biomechanical properties of tumor was shown to be changed after therapy due to necrosis and other histological changes of tumor tissue [20,21]. The OCT-based elastography (OCE) is emerging as a new perspective approach for tissue stiffness measuring (elasticity mapping) with spatial resolutions in the range 30–100 μm , suggesting several attractive advantages for imaging in clinic [22–25]. Recently, using excised breast cancer samples [26] and murine model breast cancer treated by chemotherapy [20,21], the OCE ability was demonstrated to determine different histological structures of tumor by evaluating their stiffness. For rather mechanically heterogeneous breast cancer samples studied in [26], up to 5-6 morphological constituents were segmented. Murine model 4T1 of breast cancer studied *in vivo* in [20,21,27] was characterized by somewhat simpler structure (4 main morphological components). For two different types of chemotherapy (cytotoxic with cisplatin and anti-angiogenic with bevacizumab), those tumors demonstrated the same morphological alterations (necrosis, edema, dystrophic tumor cells and viable tumor cells) with very similar characteristic stiffness ranges. Importantly, that conventional histology and the *in vivo* feasible OCE have proven to enable comparable diagnostic value from the viewpoint of characterization of microstructural/morphological alterations [27] ensuring similar accuracy of morphological segmentation ~30-50 μm , although the initial resolution of histological images was an order of magnitude higher than in OCT scans.

To verify universality of the OCE-based segmentation method and demonstrate it in another biomedical problem, the specific stiffness ranges initially established in [27] for 4T1 tumor, in this study we applied for morphological segmentation of another tumor model - murine colon

carcinoma CT26. It was treated by two different vasculature-targeted therapies - bevacizumab-based ChT and PDT, the results of the latter being assessed by OCE for the first time. In parallel, to verify universality of OCA that previously proved to be very efficient for early assessment of PDT [6,19] and radiation therapy [16], for the first time OCA was applied to assess anti-angiogenic chemotherapy. Therefore, to enable complex evaluation of tumor reaction to therapies, in this study we combined for the first time *in vivo* functional characterization (by observing blood flow alterations using OCA) with *in vivo* assessment of microstructural/morphological alterations (using OCE-segmentation) as described in the following sections.

2. Materials and methods

2.1. Multimodal OCT system

The tumor response to therapy was assessed by a multimodal OCT system (designed at the Institute of Applied Physics RAS, Nizhny Novgorod) with a central wavelength of 1310 nm, power output of 15 mW, transversal resolution of 25 μm , axial resolution of 15 μm (in air), scanning depth of up to 2 mm in air and a scanning speed is 20,000 A-scans per second [28]. The system is capable of 2D cross-polarization imaging [29], 3D angiographic visualization [15,17,30,31], as well as imaging of local strains and quantitative stiffness evaluation using compressional elastography [32–38].

2.1.1. In vivo OCA imaging

The realized OCA method can be viewed as a kind of speckle-variance approach [14], but based on the complete complex-valued amplitude (i.e. utilizing both amplitude and phase variations of the signal scattered by moving blood particles). Unlike comparing repeated OCT scans for the same position as in [14], we analyzed the signal variability by performing high-pass filtering [15,17] applying a sliding window to every group of nearly overlapped ~ 7 -8 B-scans in the recorded 3D-stack along the slow-scanning direction orthogonal to the B-scan planes. However, in the used real-time realization [17] the three steps of making the Fourier transform, high-pass filtering of the spectrum and the subsequent inverse Fourier transform were combined into a single computationally efficient operation. It consisted of time-domain convolution of the acquired OCT signal with a sliding along the slow axis pulsed function (see details in [17]). Such convolution was equivalent to sliding high-pass filtering of the overlapped scans and allowed for on-flight visualization of the vascular network “on-flight” during the acquisition of the 3D image (see the flow-chart in Fig. 1).

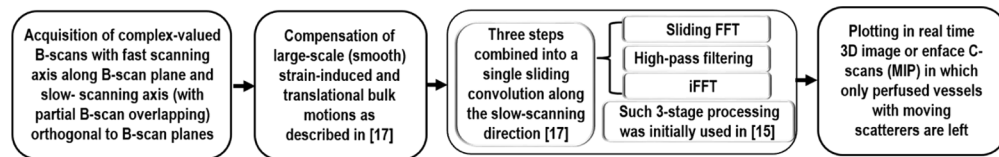


Fig. 1. Schematic of OCA data acquisition and signal processing.

The scanned volume was $2.4 \times 2.4 \times 1.5$ mm in size. For further OCE-image analysis, each obtained 3D microvascular network was represented as 2D maximum intensity projections, showing the vascular network *en-face* over the entire visualization depth.

We emphasize that the used OCA method visualizes only perfused vessels with moving scatterers in the blood flow [5]. The perfused vessel density (PVD) was chosen as a main metric due to its simplicity, robustness, and easy interpretation. PVD was calculated as the number of pixels of all vessel skeletons (i.e. central lines of skeletonized vessels) in the analyzed image area, divided by the total number of pixels in this area (see [6,16]). By analogy with our previous

animal study [5], the vascular response to the therapy was categorized as “strong” or “weak” based on the OCA examination. Strong reaction meant no visible vessels on OCA images because of significant vascular damage; weak reaction meant that a small number of vessels (the density of which was above certain pre-determined PVD threshold) were still visible post treatment, see details in [5,6].

2.1.2. In vivo OCE imaging

For assessing the tissue stiffness, we applied a realization of compressional OCT-elastography described in detail in [32–38]. OCE visualization of local strains used estimation of axial gradients of interframe phase variations of the OCT signal induced by the tissue deformation produced by the output window of the OCT probe (see the flow chart in Fig. 2). The phase gradients were estimated using the vector method [35,36], which is exceptionally robust to decorrelation distortions and other measurement noises and does not require the conventionally used phase unwrapping even for supra-wavelength displacements of scatterers. To quantify the tissue stiffness (Young’s modulus) from the reconstructed spatial distributions of strains, a translucent reference (silicone) layer with pre-calibrated stiffness (usually ~ 100 kPa) was placed on the tissue surface and was used as an optical stress sensor. A very important feature of the used method was that for estimating the tissue stiffness, we ensured the same standardized range of pressure applied to the tissue over the entire scan in all measurements, which was controlled via strain in the reference silicone layer (see details in [26,27]). The necessity of such standardization is caused by pronounced nonlinearity of stress-strain curves of biological tissues [39], for which the apparent Young modulus may vary several times for rather moderate pressures $\sim 10^0 \dots 10^1$ kPa corresponding to tissue straining within several per cent (see examples of such nonlinear curves obtained using OCE in Refs. [34,37,40,41]). Importantly, the reference silicones, exhibit fairly linear stress-strain relationships up strains \sim several tens per cent [34,37], which enables their utilization as linear stress-sensors. In what follows, similarly to [26] and [27] the standardized pressure range for estimating the tissue stiffness was 4 ± 1 kPa.

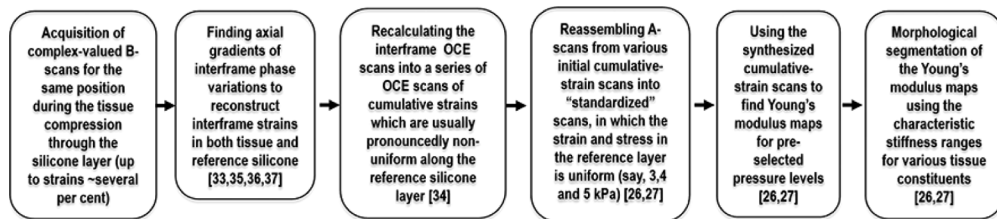


Fig. 2. Schematic of OCE data acquisition and signal processing.

In the initial individual elastographic maps the stress produced by the compressing OCT-probe window was noticeably inhomogeneous over the lateral coordinate, because the surface of studied tumors was not ideally planar and tumor stiffness could laterally vary. In view of this, in each experiment several tens of OCT images of the monotonically compressed tissue and reference layer were recorded. Then interframe strains were found and cumulative strains in the tissue and reference layer were calculated as a function of frame number. Using such many-frame sequences of cumulative strains, it was possible to re-assemble A-scans taken from cumulative-strain frames with different numbers in order to synthesize a single map of strain distribution, such that for every lateral coordinate in the synthesized image the strain and stress in the reference silicone corresponded to the desired standardized level. Such standardization was critically important for meaningful comparison of different measurements.

Further quantitative processing of the so-obtained pressure-standardized OCE images included analysis of evolution of the “stiffness spectra”, i.e., histograms (Fig. 7(a), 10(a)) showing

percentages of pixels with different stiffness on the OCE images obtained for the tumors subjected to therapies, as well as control tumors. The histograms were normalized to 100% over the total area of the chosen region of interest, so that the bin heights gave percentages of pixels corresponding to particular ranges of stiffness. As was recently shown in study [26] such stiffness spectra extracted from high-resolution OCE-maps are much more informative in comparison with conventionally discussed average stiffness values.

Finally, we applied procedures of automated morphological segmentation of the pressure-standardized OCE-images. In the recent works [21,26] such OCE-based segmentation was applied to human breast-tumor samples (for which six main morphological components were segmented) and in [27] the same method was applied *in vivo* to chemotherapy-treated murine model of breast cancer (that has simpler morphology characterized by four main histological zones). The segmentation principle is based on the revealed fact that the studied morphological components of the tissue are characterized by specific, clearly distinct ranges of the Young modulus. These ranges were determined via accurate comparison of the OCE stiffness maps with the corresponding histological sections. According to the revealed specific stiffness ranges, the OCE images were readily automatically segmented into zones that were instructively represented in different colors (see Figs. 7(b), 10(b) below). The areas of the so-segmented zones in OCE-maps demonstrated striking correlation with the areas of histological components segmented by an experienced histopathologist on conventional histological sections using QuPath image analysis software (v0.1.2) (see details in [27]). In particular, areas of different non-tumor and tumor zones comprising fairly small cell agglomerates with sizes of a few tens of microns can be segmented. In the next sections we show that similarly to [27], where details of determining the specific stiffness ranges are presented for the murine cancer model, the following four main morphological components can be segmented on the OCE-scans of tumors: (i) necrosis of tumor tissue characterized by the lowest stiffness values from 101 kPa to 230 kPa; (ii) edema of tumor tissue with stiffness values ranged from 231 kPa to 410 kPa; (iii) irreversible dystrophy of tumor cells with a stiffness range from 411 kPa to 620 kPa and (iv) viable tumor tissue that has the most rigid structure and is characterized by the highest stiffness values, over 621 kPa (Fig. 7(c), 10(c)).

2.2. *In vivo* fluorescent imaging

Tumor's blood vessels reaction to ChT and PDT was additionally visualized by fluorescent imaging. A fluorophore FITC conjugated with a dextran 2 MegaDaltons (Sigma, USA) was injected intravenously to the experimental animals in dose 50 mg/kg body weight. The study was carried out on a fluorescent stereomicroscope Axio Zoom V16 (Zeiss, Germany). For excitation of fluorescence and emission detection, the following set of filters was used: excitation 470/40 nm, emission 520/50 nm, dichroic mirror 495 nm. The fluorescent images were obtained in control tumors, on day 5th post ChT and 1st post PDT. Vascular density on the fluorescent images was determined by analogy with the OCA images.

2.3. *Animal model*

The efficiency of the OCA and OCE methods for evaluating the response to treatment was tested on murine colon carcinoma CT26 ($n = 32$ for ChT and $n = 32$ for PDT). The tumor cell suspension (200,000 cells in 20 μ l phosphate buffer) was inoculated intracutaneously into the external auricle tissue of 8-weeks old female BALB/c mice (weight of 20–22 g). An ear tumor model is characterized by a surface growth, a relatively small size (several millimeters in diameter) and good accessibility for visual examination and optical bioimaging. The present study was approved by the Research Ethics Board of the Privalzhsky Research Medical University (Nizhny Novgorod, Russia).

2.4. Chemotherapy (ChT)

The antiangiogenic drug Avastin (Bevacizumab, Roche, Switzerland) was used in the study. Animals were randomly divided into 2 groups: a control group ($n = 16$) receiving saline solution; therapeutic group ($n = 16$) receiving bevacizumab. To achieve better therapeutic effect the treatment was started on day 2 after tumor inoculation (Fig. 3), as was done in [21]. A dose of 15 mg/kg of bevacizumab was established as the most optimal for achieving inhibition of tumor growth [42]. The drug was administered intraperitoneally three times per week [20]. In total, 4 courses of drug administration were performed (Fig. 3).

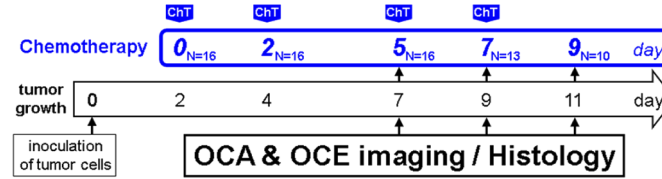


Fig. 3. Design of experiments on chemotherapy (ChT).

2.5. Photodynamic therapy (PDT)

PDT was performed on 13th day after tumor inoculation when the tumor size reached 3-3.5 mm in diameter (Fig. 4). Photosensitizer “Photodithazin” (N-dimethylglucamine salt of Chlorine E6, Veta-Grand, Russia) was administered intravenously in dose 5 mg/kg of body weight and irradiated after one hour with a diode laser (659 nm) with irradiance rates 100 mW/cm² and total irradiance 100 J/cm². That PDT regime was demonstrated to occur vascular-targeted action [6,43]. Animals were randomly divided into 2 groups: treated by PDT ($n = 16$) and untreated control ($n = 16$).

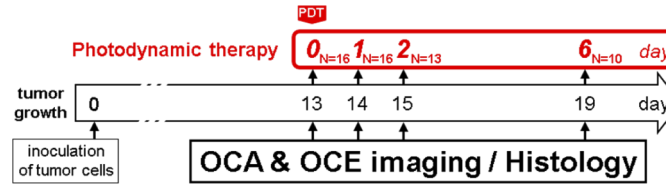


Fig. 4. Design of experiments on photodynamic therapy (PDT).

2.6. Conventional assessment of tumor response to therapies

Currently, the evaluation of the response of an experimental tumor to treatment includes monitoring the tumor size changes and determining the morphological regression of the tumor by histological examination [1].

2.6.1. Estimation of tumor volume dynamics

The tumor size was measurement with a caliper on days 2, 5, 7 and 9 for ChT and before PDT, 24 hours, 2 and 6 days after PDT. Tumor volume (V , mm³) was as $\pi/6 a*b*c$, where a is the length of the tumor, b is its width and c is the height [44]. Tumor growth inhibition coefficient (TGI) as a standard for animal anti-tumor therapy efficacy study was estimated [45]:

$$\%TGI = \left(1 - \frac{(V_T - V_{T0})/V_{T0}}{(V_C - V_{C0})/V_{C0}} \right) \times 100\%, \quad (1)$$

where subscripts “T” and “C” correspond to the treated and control groups and subscript “0” denotes the initial tumor volume. The relation of this coefficient with tumor-volume

decrease/increase is as follows: $TGI > 100\%$ - tumor volume decreased (effective treatment); $TGI \sim 100\%$ - tumor volume did not change, $TGI < 100\%$ tumor volume increased (ineffective treatment).

2.6.2. Histopathology

After *in vivo* multimodal OCT studies, for histological validation, at days 5, 7 and 9 after ChT and 1, 2 and 6 days after PDT, three animals from each of the studied groups were sacrificed and tumor nodes were resected. For co-location of histology with the OCT scans, positions of the latter on the tumors were marked by histological ink. Tumor samples were fixated in 10% neutral buffered formalin. To study tumor tissue morphology, several cross sections were made from the tumor center and stained with hematoxylin and eosin (H&E). Histopathology examination included the identification of viable tumor cells (not damaged by therapy), necrosis, edema and dystrophic tumor cells (pathological mitoses, cells with karyopcnosis/karyorexis/karyolysis/vacuolization of the nuclei). Validation of blood vessels integrity was carried out immunohistochemically (IHC) staining again vascular endothelium (CD31) on day 5th post ChT and 1st post PDT. Quantitative analysis of the vascular density on IHC images was performed using ImageJ software (National Institutes of Health, USA) as the number of pixels with high signal from stained vessels in the analyzed image area, divided by the total number of pixels in this area.

The histological slices were prepared using a Leica RM 2245 Rotary Microtome, and studied on transmitted light microscope Leica DM2500 DFC (Leica Microsystems, Germany), equipped with a digital camera.

2.7. Statistical analysis

The statistical significance of differences in the tumor volume changes, the vessels density and the stiffness differences between the control non-treated and treated (ChT or PDT) tumors was calculated by the student's t-test. All the results were expressed as mean \pm SD. In all cases, the differences were considered statistically significant when $p < 0.05$. Pearson correlation coefficient (r) was calculated to determine the correlation between (i) vessels density on the OCA and fluorescent images, (ii) the area of necrosis revealed by histology and OCE images, (iii) the areas of viable tumor cells revealed by histology and OCE images.

The statistical data processing was done in MS Excel 2010 with a public domain software plugin for statistical analysis STATISTICA 10 (StatSoft, Inc., Tulsa, Oklahoma).

3. Results

3.1. Tumor response evaluation to anti-angiogenic chemotherapy

3.1.1. Conventional assessment

The dynamic of tumors growth (see Fig. 5(a)) demonstrates slight inhibition of tumor volume on the 9th day of observation ($TGI_{9d} = 37\text{-}54\%$).

According to histopathology assessment, the dominance of viable tumor cells and appearance of weak edema was shown in control group on day 9. Histopathology examination of tumors on day 5 after ChT revealed severe blood vessels injuries: (i) desquamation of the endothelium of the vascular wall and (ii) moderate plethora of blood vessels and (iii) hemorrhages. Severe edema as a result of blood vessels reaction was also observed. Only small clusters of viable tumor cells (about 10-20% of the total tissue area) and dystrophic tumor cells (about 5-15% of the total tissue area) were revealed (see Fig. 5(b)). The development of these histopathological changes was observed up to day 9. In addition, areas of ischemic necrosis of the tumor cells (whose percentage on day 9 reached 35-42%) were observed on days 7 and 9.

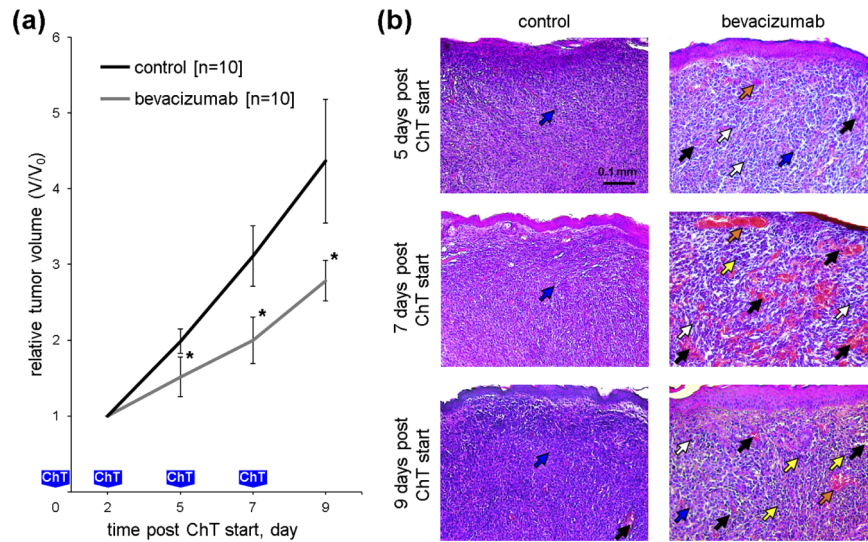


Fig. 5. Effect of ChT on tumor CT26. (a) Monitoring of relative tumor volume changes for bevacizumab (n = 10) and control (n = 10) groups. Data are shown as mean \pm SD. Asterisks * denote statistically significant difference between bevacizumab and control groups, $p \leq 0.05$. (b) Histological images (H&E) of control and bevacizumab-treated tumors. Blue arrows indicate viable tumor cells; orange arrows indicate desquamation of the endothelium of the vascular wall and moderate plethora of blood vessels; black arrows indicate hemorrhages and edema; yellow arrows indicate ischemic necrosis of the tumor cells.

3.1.2. In vivo angiographic monitoring of ChT-induced changes

Figure 6(a) demonstrates OCA images of perfused tumor microvasculature at different time points post ChT. Control group demonstrated well-developed blood vessels network on OCA images throughout all observation time period (Fig. 6(a)). Unlike the control tumors, bevacizumab-treated tumors on the 5th day showed weak microvascular damage manifested as partial blood vessels disappearance (Fig. 6(a)). On days 7 and 9, a significant regression of the vasculature (severe microvascular damage) was observed in the OCA images and confirmed by quantitative analysis (Fig. 6(d)). The fluorescent images (Fig. 6(b)), IHC images (Fig. 6(c)) and quantitative analysis of the all types of images (Fig. 6(d), (e)) confirm that bevacizumab-treated tumors have low dense of perfused vessels.

3.1.3. In vivo elastographic monitoring of ChT-induced changes

The stiffness percentage graph for the control group (see Fig. 7(a)) shows weakly varying tumor stiffness with dominating high values >800 kPa at all time points. In the bevacizumab-treated group, there was a dramatic decrease in stiffness values (down to ~ 300 kPa) on day 5, and a further decrease in stiffness on days 7 and 9. At all time points the characteristic stiffness values for bevacizumab-treated tumors were 3-4 times smaller than for the control group.

Segmentation of the *in vivo* obtained OCE images (Fig. 7(b)) and their quantitative analysis (Fig. 7(c)) demonstrate pronounced changes in histological structure of tumors under therapy in contrast to the control group. In the control tumors, segmented OCE images consist of weakly varying zones of viable tumor cells (occupying more than 95% of the tumor area) with small areas of dystrophic tumor cells (occupied up to 5%). In contrast, segmented OCE images of bevacizumab-treated tumors demonstrate strongly reduced zones of viable tumor cells and the appearance of large areas of edema (occupied 62%, 58% and 43% at the corresponding time

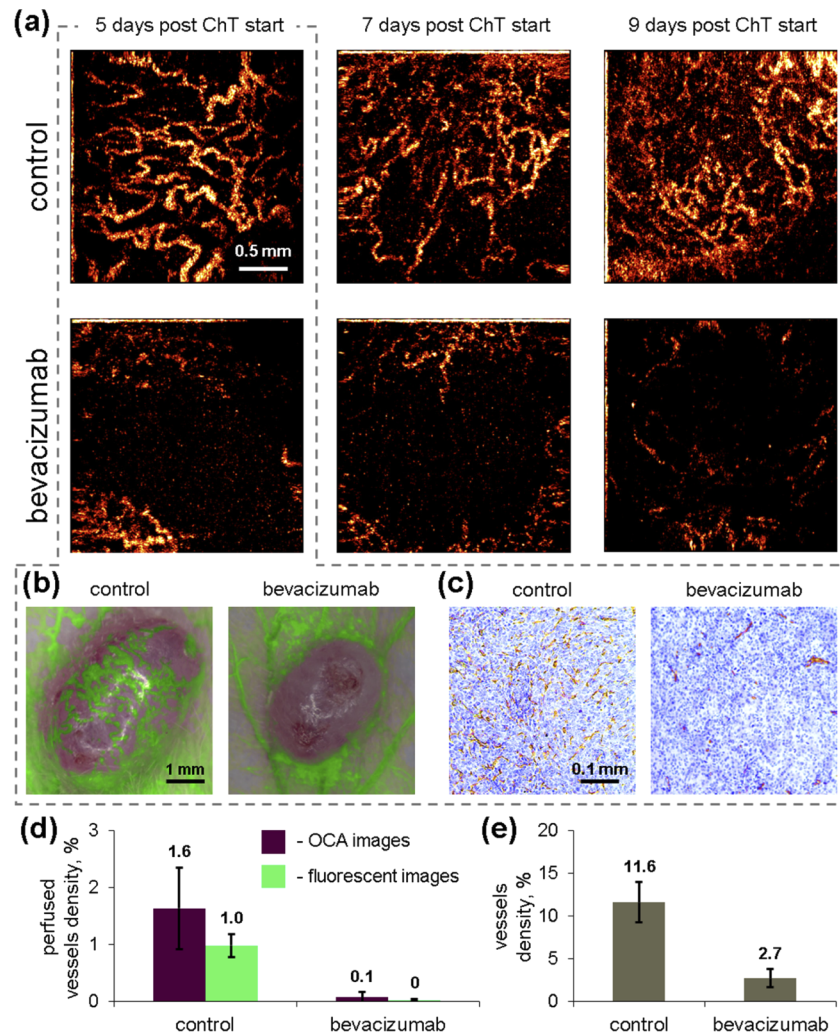


Fig. 6. Monitoring of tumor's blood vessel reaction to anti-angiogenic ChT with bevacizumab by means of (a) *in vivo* real time OCA imaging; (b) corresponding fluorescent images and (c) IHC images (CD31 staining of blood vessels) in control tumors and 5 days post start of ChT. (d) perfused vessels density, determined on OCA and fluorescent images, (e) vascular density, determined on IHC images.

points), dystrophic tumor cells (occupied 15%, 10% and 6% at corresponding time point) and steadily growing necrosis areas (occupied 4%, 15% and 34% at corresponding time point).

Pearson correlation coefficient shows a strong correlation between the histological images and segmented OCE images for the areas of viable tumor cells ($r = 0.94$) and necrosis ($r = 0.98$). This strong correlation confirms a high degree of consistency between histologically-revealed morphological changes in the tissue and changes in stiffness in OCE images.

Figure 7(c) demonstrates that bevacizumab treatment led to decrease in the number of perfused blood vessels in OCA images already at 5th day post ChT start. This resulted in severe edema that was clearly revealed by OCE. On 7th day and later, the strong disruption of blood supply (detected by OCA) caused pronounced growth of necrosis areas, which was clearly visualized by OCE.

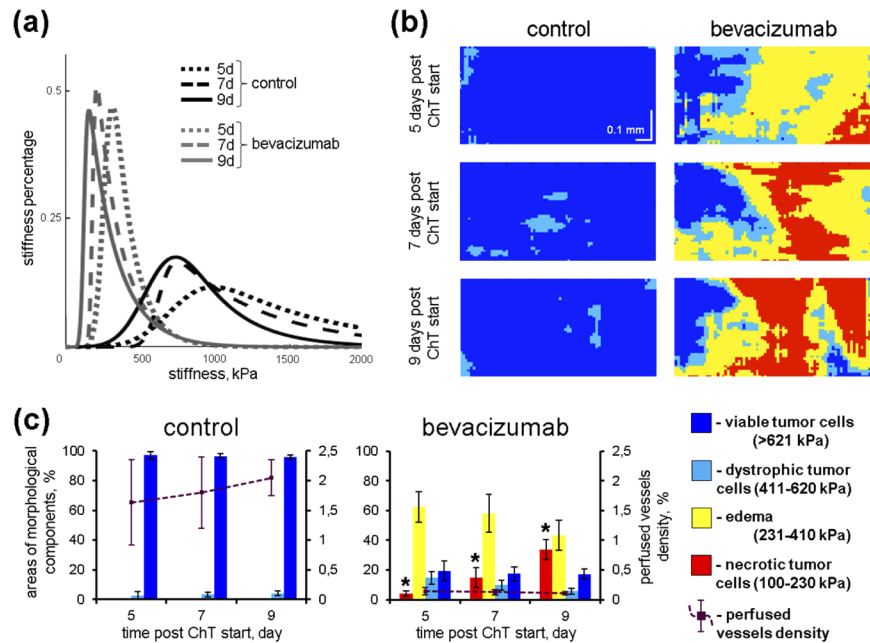


Fig. 7. *In vivo* OCE monitoring of tumor response to ChT for control and bevacizumab-treated tumors at 3 time points: (a) Stiffness-percentage graphs illustrating the shift of the normalized stiffness spectrum (total area under the curve is 100%) to lower values for bevacizumab-treated tumors (gray lines) in compared with control tumor (black lines); (b) Segmented OCE images demonstrating various tumor zones (viable tumor cells, dystrophic tumor cells, edema and necrosis of tumor cells); (c) Percentages of pixels (left vertical axes) belonging to different stiffness ranges for the control group and bevacizumab-treated one (blue, light blue, yellow and red columns). The dashed purple lines and right vertical axes show percentage of perfused vessels density. Asterisk * indicates statistically significant difference in the areas of necrotic tumor cells between the bevacizumab and control groups, $p \leq 0.05$. The color palette on the right indicates the stiffness ranges corresponding to each color in the bar graphs and segmented OCE images.

Thus, OCE was able to detect ChT-induced microstructure alterations *in vivo* with high sensitivity. Segmented OCE images (Fig. 7(b)) allow one to accurately determine in real time the presence and proportion of destructive changes in the structure of the tumor as a result of ChT. The “stiffness spectra” evolution (similar to the graphs in Fig. 7(a)) clearly and quantitatively reflect the changes that occur in tumor tissue in response to ChT.

3.2. Tumor response evaluation to vessel-targeted PDT

To complement the above-presented results of tumor response to ChT, this section demonstrates the usefulness and universality of the OCA and OCE approaches for assessment of the tumor response to PDT representing another type of vascular-targeted therapy with an essentially different mechanism of action.

3.2.1. Conventional assessment

Figure 8(a) demonstrates significant decrease in the tumor volumes by 24 hrs after PDT for all treated tumors in comparison with untreated ones. However, on day 6 post-PDT only 5 of 8 PDT-treated tumors had statistically significant smaller volumes compared to control tumors with TGI coefficient 160-194%.

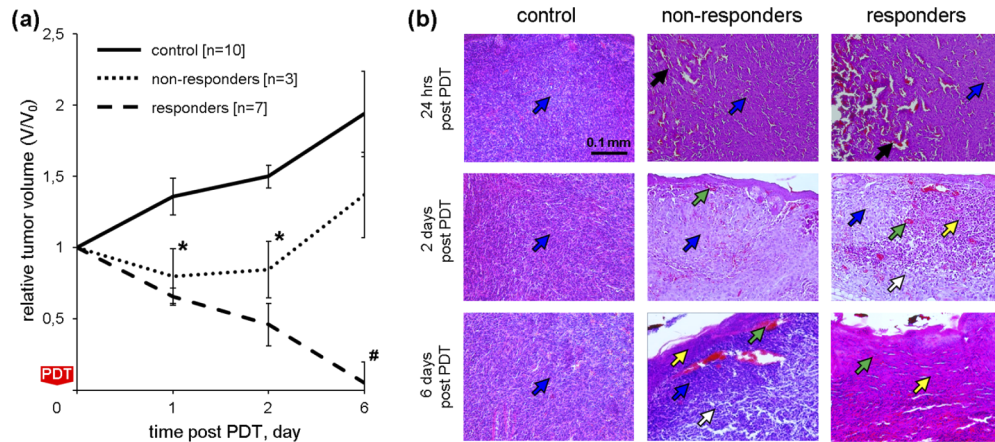


Fig. 8. Effect of PDT on CT26. (a) Monitoring of relative tumor volume changes for responders ($n = 7$), non-responders ($n = 3$) and control ($n = 10$) tumors. Data are shown as mean \pm SD. Tumor growth was statistically significantly inhibited by PDT in the responders. Asterisk * denotes statistically significant difference of responders and non-responders from control ones ($p \leq 0.05$) and # denotes statistically significant difference of responders from non-responders ($p \leq 0.05$). (b) H&E histological images of CT26 tumors. Black arrows indicate hemorrhage; green arrows indicate vascular thrombosis; blue arrows indicate viable tumor cells; white arrows show clusters of dystrophic tumor cells; yellow arrows show necrosis of tumor cells.

Histological examination of PDT treated tumors reveal alterations similar to those in the bevacizumab-treated tumors, such as necrosis, edema, dystrophic and viable tumor cells (Fig. 8(b)). Thrombosis of blood vessels and hemorrhage, the weak edema and the clusters of dystrophic tumor cells were detected already at 24 hours after PDT. At day 2 post PDT, the regions of these morphological changes increased due to extensive areas of necrosis and dystrophic tumor cells. At day 6 post-PDT a total (100%) necrosis was observed in 5 of 8 tumors. These tumors were categorized as responders, based on classifications from [5]. At day 6 post PDT, 3 of 8 tumors had 20-30% of viable tumor cells, 10-20% of necrotic of tumor cells and also clusters of dystrophic tumor cells. These tumors were categorized as non-responders [5].

3.2.2. In vivo angiographic monitoring of PDT-induced changes

Control tumors demonstrated well-developed blood vessels network on OCA images throughout all observation time period (Fig. 9(a), upper row). In contrast, already in 6 hours post PDT only a few vessels were visualized by OCA in case of responders. Importantly, complete and irreversible tumor's blood vessels disappearance was shown in 24 hours post PDT in the case of responders in OCA images (Fig. 9(a), lower row). Conversely, only partial disappearance of tumor's blood vessels was observed in 24 hours post-PDT in case of non-responders (Fig. 9(a), middle row), which was confirmed by quantitative analysis of the images (Fig. 9(d)). This result well agrees with our earlier studies [5,6], where OCA criteria of PDT success were formulated based on perfused vessel density (PVD): zero PVD (i.e., no perfused vessels visible on the OCA image) in the tumor and $PVD < 1\%$ in the peri-tumorous region in 24 hours post PDT.

The fluorescent (Fig. 9(b)) and IHC (Fig. 9(c)) images and their quantitative analysis confirm that PDT damages blood vessels and interrupts blood perfusion (Fig. 9(d), (e)). Pearson correlation between vessel density on the fluorescent images and OCA images is $r = 0.952$. Thus, despite quite different anti-angiogenic action mechanisms for PDT and bevacizumab-based ChT,

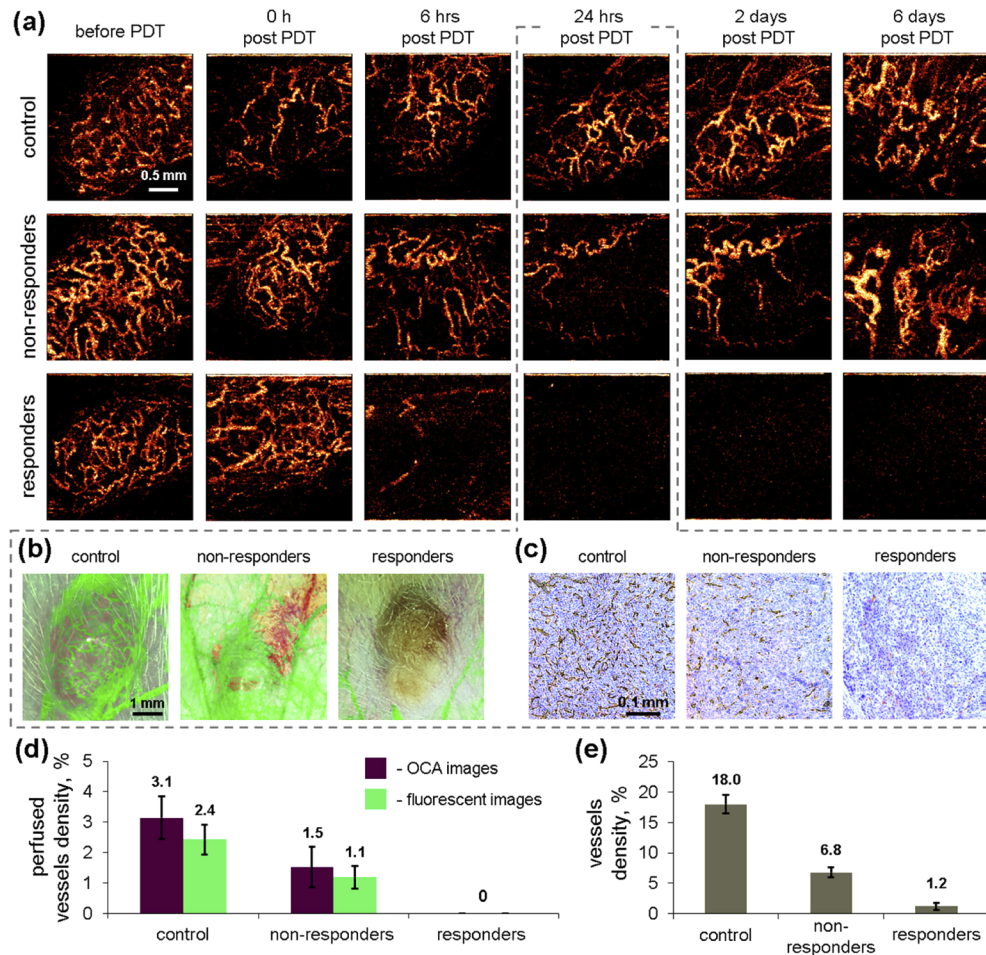


Fig. 9. Monitoring of early tumor's blood vessels reaction to vascular-targeted PDT by means of (a) *in vivo* real time OCA imaging, (b) corresponding fluorescent images and (c) IHC images (by CD31 staining) of blood vessels in control tumors and 24 hours post PDT, (d) – perfused vessels density, determined on OCA and fluorescence images, (e) vascular density, determined on IHC images.

OCA has proved to be very sensitive to blood perfusion interruption regardless of the treatment type, which indicates the universality of the OCA approach.

3.2.3. In vivo elastographic monitoring of PDT-induced changes

Similarly to section 3.1.3, the stiffness percentage graphs for the control tumor (Fig. 10(a), black line) show weakly varying and rather high tumor high stiffness (mostly >800 kPa) during all observation period. In the treated group, no significant changes in the stiffness spectra were observed in early time points post PDT (0 and 6 hours) by means of OCE. Then, rather pronounced differences in stiffness of responders to PDT in comparison to both control group and non-responders were noted at days 1, 2 and 6 post PDT (Fig. 10(a)). The stiffness-percentage graphs show that the stiffness shift to lower values starts from 24 hours for responders in contrast to non-responders. At day 6 post PDT the responders have much greater content of components with

low stiffness <400 kPa (Fig. 10(a), dashed line) in comparison with non-responders (Fig. 10(a), dotted line).

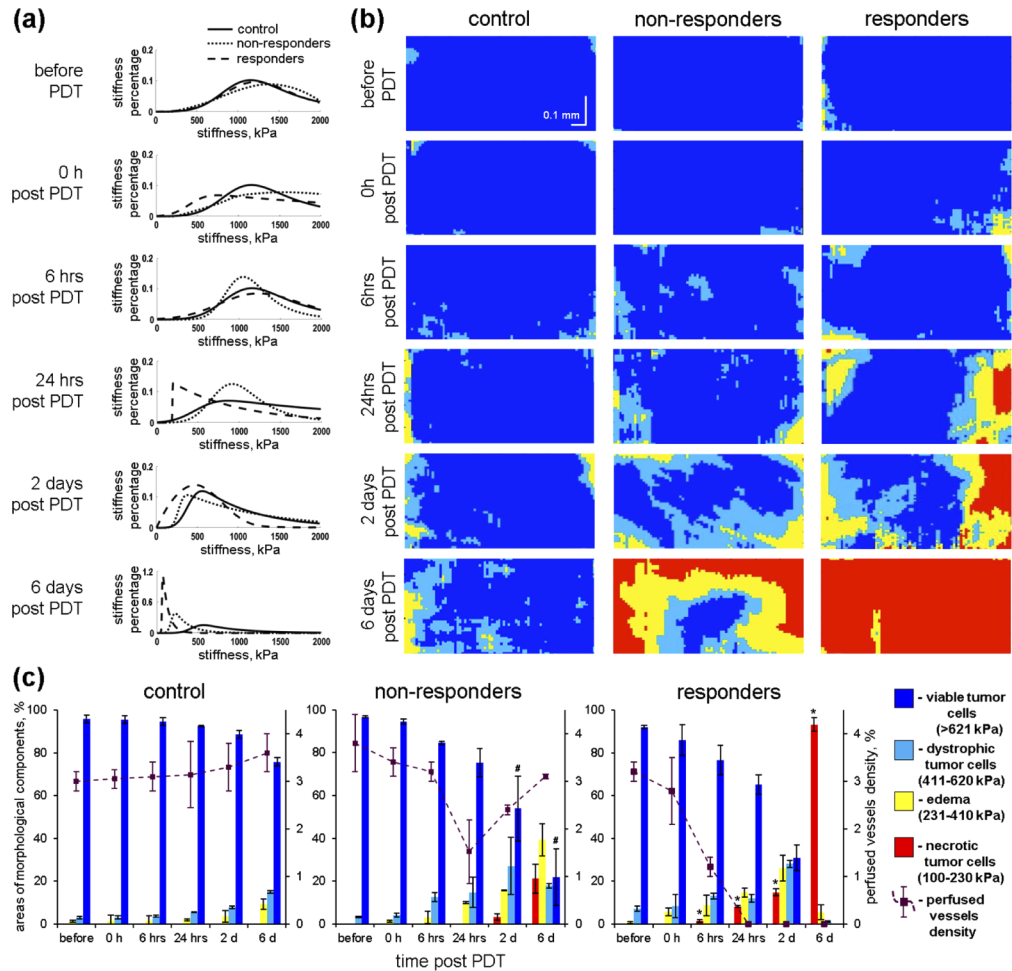


Fig. 10. *In vivo* OCE monitoring of tumor response to PDT: (a) Stiffness-percentage graphs illustrating the shift of the stiffness spectrum (total area under the curves is 100%), (b) Segmented OCE images demonstrated various tumor zones (viable tumor cells, dystrophic tumor cells, edema and necrosis of tumor cells); (c) Percentage of pixels (left vertical axes) belonging to the specific stiffness ranges for different morphological zones (blue, light blue, yellow and red columns). The dashed purple lines and right vertical axes show percentage of perfused vessels density. No significant stiffness changes were noted in the control tumors with strong dominance of viable tumor zone, whereas for non-responders and responders, the most stiff viable tumor zones (blue color) in (b) and (c) strongly diminished at day 6 post PDT, when responders showed total necrosis (red color) on the segmented OCE images. Asterisk * denotes statistically significant difference of responders from non-responders in percentage of the necrosis area, $p \leq 0.05$. # denotes statistically significant difference of non-responders from responders in percentage of the viable tumor cells, $p \leq 0.05$.

Segmented OCE images (Fig. 10(b)) and their quantitative analysis (Fig. 10(c)) demonstrate *in vivo* changes in histological structure of tumors subjected to PDT (central and right columns in Fig. 10(b)). Segmented OCE-images of control tumors during the development demonstrate prevalent viable tumor cells (occupied 95-65% in corresponding time period). Only small areas

of dystrophic tumor cells (3-28% in corresponding time period) and edema (no more than 14%) are visualized by OCE. Normally, spontaneous degenerative changes of tumor cells are occur during tumor development. Figure 10(b) (2nd and 3rd rows from top) shows, that at early time points (0 and 6 hours), there was no significant difference in the percentages of viable tumor cells area between control, responders and non-responders.

In contrast, for days 1, 2 and 6, tumor stiffness markedly differed for control and treated animals (lower 3 rows in Fig. 10(b) and Fig. 10(c)). Importantly, that significant difference was already observed when comparing tumor stiffness for responders and non-responders at 24 hours. The percentage of necrosis area featuring very low rigidity (less 230 kPa) was significantly higher for responders compared to non-responders at 24 hours, 2 and 6 days (Fig. 10(c)). On segmented OCE-images of responders, in 24 hours post PDT in addition to edema and dystrophic tumor cells, a distinct area of necrosis (occupied ~8%) was detected and then pronounced extension of the necrosis area was observed at day 2 (up to 15%) with maximum at day 6 (~93%). For non-responders, the zone of viable tumor cells exhibited clear reduction only at days 2 and 6 post PDT with clear appearance of the necrotic tumor cells (~21% at day 6), which was much less than in responders (~93%). Additionally, zone of viable tumor cells visualized in non-responders was statistically significantly higher compared to responders at day 2 ($54 \pm 15\%$ vs $31 \pm 6\%$, respectively) and 6 ($22 \pm 13\%$ vs 0%, respectively).

These OCE results are consistent with histology for all four identified tumor zones (viable tumor tissue, dystrophic tumor cells, edema and necrosis of tumor tissue). Pearson correlation coefficient shows a strong correlation between the area of necrosis revealed by histology and OCE: for responders $r = 0.97$ ($p < 0.001$) and for non-responders $r = 0.84$. In addition, strong correlation was shown between the histological images and segmented OCE images for the areas of viable tumor cells: for responders $r = 0.98$ ($p < 0.001$) and for non-responders $r = 0.92$. This correlation is shown for the first time and demonstrates the high degree of agreement between the morphological changes in the tissue and stiffness changes on the OCE images. Consequently, based on the segmented OCE images, histological structure of the tissue can be assessed.

Interrelation between the vascular reaction and stiffness changes after PDT is clear from Fig. 10(c). Blood flow disruption (decrease of perfused vessels density on OCA images) at 6 hrs post PDT in case of responders is pronouncedly stronger than for non-responders, whereas the moderate stiffness decrease (because of edema formation) is not that different for responders and non-responders. Then at 24 h and later, complete disappearance of perfused blood vessels on OCA images for responders is accompanied by pronounced necrosis formation and dramatic decrease in stiffness on OCE images. For non-responders, these stiffness alterations are much weaker, whereas the vascular network even begins to restore after 24 h.

Thus, *in vivo* OCE segmentation allows one to accurately determine in real time the presence and proportion of the necrotic zone in case of successful PDT in the early period within 24 hours post PDT. In case of unsuccessful treatment, the OCE-based segmentation accurately detects remaining viable tumor cells in 6 days post PDT. It can be emphasized that despite quite different anti-angiogenic mechanisms of bevacizumab and PDT, the similar histological structure alterations such as necrosis, edema, viable and dystrophic tumor cells were revealed.

4. Discussion and conclusions

Presently, RECIST remains the most common conventional way to evaluate tumor response to cytotoxic chemotherapy [2]. However, new methods of anti-tumor therapies, which are targeted at blood vessels rather than directly at the tumor cells, require new approaches for tumor response evaluation [1]. In this study, we compare two different vascular-targeted therapies that indirectly kills tumor cells through blood supply injury: (i) anti-angiogenic with bevacizumab and (ii) photodynamic therapy. For the first time we applied in combination OCA and OCE to test the ability these optical methods to *in vivo* predict tumor response. Another goal of the study was to

estimate the universality of these approaches by applying each of these methods to another type of tumor and another type of therapy in comparison with previous, partially similar, applications of OCA and OCE [5,6,19,26,27].

It is well known that the action of antiangiogenic chemotherapy is aimed at suppressing neoangiogenesis of tumor tissue [46] and vascular-targeted PDT has thrombogenic effect on blood vessels [12]. Despite quite different mechanisms of anti-angiogenic action of bevacizumab and PDT, similar histological structure alterations such as necrosis, edema, viable and dystrophic tumor cells were revealed in the present study. OCA was demonstrated to be very sensitive to blood perfusion interruption after both therapies. Our recent studies demonstrated that OCA is very sensitive to blood perfusion and is a helpful and reliable tool for prediction of PDT response based on vascular reaction within 24 hours post PDT [5,6]. However, in this study for the first time OCA was applied for monitoring of tumor vasculature post bevacizumab treatment. Complete disappearance of tumor blood vessels was shown by OCA under bevacizumab therapy. Well-developed blood vessels network normally characterize untreated tumors. Appearance of avascular zones gives evidence that something wrong with blood vessels. It should be pointed out that although OCA is well suited to characterize functional state of blood vessels (presence/absence of perfusion) it is not sensitive to microstructural/morphological alterations of tissue.

In this context, our recent studies [27] on breast cancer tumor model 4T1 treated by cisplatin and bevacizumab demonstrated high sensitivity of OCE to histological structure alterations with the possibility to evaluate percentages of necrotic and viable tumor cells via automated segmentation of OCE images. In addition to OCE-studies of mechanical and histological heterogeneity of breast cancer samples [26] and model tumor 4T1 [20,21,27], the present study further extends the application range of the OCE-based segmentation using another tumor model (CT26) and another anti-tumor therapy (PDT). The obtained results has confirmed that OCE is a rather universal and highly useful tool, enabling detection of tumor stiffness decrease accompanying the appearance of edema, dystrophic and necrotic tumor cells independently of the reason of cell death.

Therefore, OCA and OCE methods complement each other and in combination bode well for assessment of tumor response to therapies, including vascular-targeted therapy. Because blood vessel destruction occurs earlier than histological changes, OCA can be helpful in early time period post therapies. In case of PDT, OCA revealed the first blood vessels reaction as early as 6 hours post therapy with fully developed reaction in 24 hours. This was confirmed by fluorescent imaging in 24 hours post PDT. Our present OCA finding are in a good agreement with independent study [47], in which a significant reduction in blood flow was observed as early as 6 hours after PDT by Laser Doppler technique. Additionally, in [47] electron micrographs revealed erythrosthesis in tumor microvessels starting as early as 2 hours after treatment and complete occlusion of blood vessels by 12 hours.

In case of bevacizumab, our OCA imaging indicated significant reduction in blood vessel density at day 5, which was additionally verified by IHC and fluorescent imaging. These findings agree with study [48], where bevacizumab-induced reduction in blood vessels density was demonstrated by invasive IHC investigation. All previous studies devoted to bevacizumab therapy were focused on the blood vessel characterization [48,49], although based on other methods than OCA. To the best of our knowledge, so far, there were no studies focused on detailed visualization of morphological alterations in the tumor structure under bevacizumab therapy. In the present study, for the first time OCE-based segmentation was used to investigate morphological alterations in the tumors in parallel with the OCA imaging of perfusion. A severe edema, as well as tumor necrosis and dystrophy were revealed *in vivo* by OCE and confirmed by histopathology. Such histology-like segmentation of OCE images allowed us to perform accurate real-time longitudinal monitoring of the appearance and proportion of morphological alterations.

To summarize, this study demonstrates that both OCA and OCE are the promising non-invasive, label-free and real-time approaches allowing one to monitor early changes in the tumor after different therapies and assess the treatment efficacy. Universality of these approaches was demonstrated on different types of therapies: vascular-targeted PDT and anti-angiogenic chemotherapy, as well as cytotoxic chemotherapy in previous studies [20,27]. Independent of the therapy type, OCA is able to visualize reduction of blood vessels density. In turn, OCE is able to visualize and quantify the tumor structure alterations (necrosis, edema, dystrophic tumor cells and viable tumor cells). Thus, the above-presented results together with our recent OCE-based studies [20,21,26,27,38] confirm that the OCE-segmentation suggests an attractive alternative to segmentation of conventional histological images, enabling previously inaccessible *in vivo* monitoring of histological structure of biological tissues for a broad range of oncological and non-oncological applications without taking multiple biopsies.

Funding

Russian Foundation for Basic Research (18-32-00608_mol_a, 18-42-520018, 19-315-90087, 19-32-90110).

Acknowledgments

The quantitative assessment of OCE stiffness maps and assessment of tumor response to PDT was funded by RFBR according to the research project No 18-32-00608_mol_a. Development of the method of obtaining pressure-standardized OCE images by reassembling individual OCT-scans was supported by RFBR project No 18-42-520018. AAP and AAS acknowledge the support by RFBR PhD-scholarship projects No 19-315-90087 in part of the development of the approach to *in vivo* OCE assessment of tumor response to chemotherapy and No 19-32-90110 in part of optimization of the OCE-segmentation algorithm, respectively.

Disclosures

The authors declare that there are no conflicts of interest related to this article.

References

1. H. Kang, H. Y. Lee, K. S. Lee, and J. H. Kim, "Imaging-based tumor treatment response evaluation: review of conventional, new, and emerging concepts," *Korean J. Radiol.* **13**(4), 371–390 (2012).
2. E. A. Eisenhauer, P. Therasse, J. Bogaerts, L. H. Schwartz, D. Sargent, R. Ford, J. Dancey, S. Arbuck, S. Gwyther, M. Mooney, L. Rubinstein, L. Shankar, L. Dodd, R. Kaplan, D. Lacombe, and J. Verweij, "New response evaluation criteria in solid tumours: revised RECIST guideline (version 1.1)," *Eur. J. Cancer* **45**(2), 228–247 (2009).
3. V. Demidov, L. A. Matveev, O. Demidova, A. L. Matveyev, V. Y. Zaitsev, C. Flueraru, and I. A. Vitkin, "Analysis of low-scattering regions in optical coherence tomography: applications to neurography and lymphangiography," *Biomed. Opt. Express* **10**(8), 4207–4219 (2019).
4. B. A. Standish, K. K. Lee, X. Jin, A. Mariampillai, N. R. Munce, M. F. Wood, B. C. Wilson, I. A. Vitkin, and V. X. Yang, "Interstitial Doppler optical coherence tomography as a local tumor necrosis predictor in photodynamic therapy of prostatic carcinoma: an *in vivo* study," *Cancer Res.* **68**(23), 9987–9995 (2008).
5. M. A. Sirotkina, L. A. Matveev, M. V. Shirmanova, V. Y. Zaitsev, N. L. Buyanova, V. V. Elagin, G. V. Gelikonov, S. S. Kuznetsov, E. B. Kiseleva, A. A. Moiseev, S. V. Gamayunov, E. V. Zagaynova, F. I. Feldchtein, A. Vitkin, and N. D. Gladkova, "Photodynamic therapy monitoring with optical coherence angiography," *Sci. Rep.* **7**(1), 41506 (2017).
6. M. A. Sirotkina, A. A. Moiseev, L. A. Matveev, V. Y. Zaitsev, V. V. Elagin, S. S. Kuznetsov, G. V. Gelikonov, S. Y. Ksenofontov, E. V. Zagaynova, F. I. Feldchtein, N. D. Gladkova, and A. Vitkin, "Accurate early prediction of tumour response to PDT using optical coherence angiography," *Sci. Rep.* **9**(1), 6492 (2019).
7. M. Muhsin, J. Graham, and P. Kirkpatrick, "Bevacizumab," *Nat. Rev. Drug Discov.* **3**(12), 995–996 (2004).
8. N. Ferrara, K. J. Hillan, H. P. Gerber, and W. Novotny, "Discovery and development of bevacizumab, an anti-VEGF antibody for treating cancer," *Nat. Rev. Drug Discovery* **3**(5), 391–400 (2004).
9. B. W. Henderson and T. J. Dougherty, "How does photodynamic therapy work?" *Photochem. Photobiol.* **55**(1), 145–157 (1992).
10. A. M. Fisher, A. L. Murphree, and C. J. Gomer, "Clinical and preclinical photodynamic therapy," *Lasers Surg. Med.* **17**(1), 2–31 (1995).

11. J. M. Dąbrowski, B. Pucelik, A. Regiel-Futyr, M. Brindell, O. Mazuryk, A. Kyzioł, G. Stochel, W. Macyk, and L. G. Arnaut, "Engineering of relevant photodynamic processes through structural modifications of metallotetrapyrrolic photosensitizers," *Coord. Chem. Rev.* **325**, 67–101 (2016).
12. B. Chen, B. W. Pogue, I. A. Goodwin, J. A. O'Hara, C. M. Wilmot, J. E. Hutchins, P. J. Hoopes, and T. Hasan, "Blood flow dynamics after photodynamic therapy with verteporfin in the RIF-1 tumor," *Radiat. Res.* **160**(4), 452–459 (2003).
13. T. Jiang, A. Kambadakone, N. M. Kulkarni, A. X. Zhu, and D. V. Sahani, "Monitoring response to antiangiogenic treatment and predicting outcomes in advanced hepatocellular carcinoma using image biomarkers, CT perfusion, tumor density, and tumor size (RECIST)," *Invest. Radiol.* **47**(1), 11–17 (2012).
14. A. Mariampillai, M. K. K. Leung, M. Jarvi, B. A. Standish, K. Lee, B. C. Wilson, A. Vitkin, and V. X. D. Yang, "Optimized speckle variance OCT imaging of microvasculature," *Opt. Lett.* **35**(8), 1257–1259 (2010).
15. L. A. Matveev, V. Y. Zaitsev, G. V. Gelikonov, A. L. Matveyev, A. A. Moiseev, S. Y. Ksenofontov, V. M. Gelikonov, M. A. Sirotkina, N. D. Gladkova, V. Demidov, and A. Vitkin, "Hybrid M-mode-like OCT imaging of three-dimensional microvasculature in vivo using reference-free processing of complex valued B-scans," *Opt. Lett.* **40**(7), 1472–1475 (2015).
16. A. V. Maslennikova, M. A. Sirotkina, A. A. Moiseev, E. S. Finagina, S. Y. Ksenofontov, G. V. Gelikonov, L. A. Matveev, E. B. Kiseleva, V. Y. Zaitsev, E. V. Zagaynova, F. I. Feldchtein, N. D. Gladkova, and A. Vitkin, "In-vivo longitudinal imaging of microvascular changes in irradiated oral mucosa of radiotherapy cancer patients using optical coherence tomography," *Sci. Rep.* **7**(1), 16505 (2017).
17. A. Moiseev, S. Ksenofontov, M. Sirotkina, E. Kiseleva, M. Gorozhantseva, N. Shakhova, L. Matveev, V. Zaitsev, A. Matveyev, E. Zagaynova, V. Gelikonov, N. Gladkova, A. Vitkin, and G. Gelikonov, "Optical coherence tomography-based angiography device with real-time angiography B-scans visualization and hand-held probe for everyday clinical use," *J. Biophotonics* **11**(10), e201700292 (2018).
18. P. Gong, S. Es'haghian, K. A. Harms, A. Murray, S. Rea, B. F. Kennedy, F. M. Wood, D. D. Sampson, and R. A. McLaughlin, "Optical coherence tomography for longitudinal monitoring of vasculature in scars treated with laser fractionation," *J. Biophotonics* **9**(6), 626–636 (2016).
19. E. V. Gubarkova, F. I. Feldchtein, E. V. Zagaynova, S. V. Gamayunov, M. A. Sirotkina, E. S. Sedova, S. S. Kuznetsov, A. A. Moiseev, L. A. Matveev, V. Y. Zaitsev, D. A. Karashtin, G. V. Gelikonov, L. Pires, A. Vitkin, and N. D. Gladkova, "Optical coherence angiography for pre-treatment assessment and treatment monitoring following photodynamic therapy: a basal cell carcinoma patient study," *Sci. Rep.* **9**(1), 18670 (2019).
20. A. A. Plekhanov, E. V. Gubarkova, A. A. Sovetsky, V. Y. Zaitsev, L. A. Matveev, A. L. Matveyev, L. B. Timofeeva, S. S. Kuznetsov, E. V. Zagaynova, N. D. Gladkova, and M. A. Sirotkina, "Optical Coherence Elastography for Non-Invasive Monitoring of Tumor Elasticity under Chemotherapy: Pilot Study," *Sovrem. Tehnol. Med.* **10**(3), 43 (2018).
21. A. A. Plekhanov, M. A. Sirotkina, A. A. Sovetsky, E. V. Gubarkova, E. B. Kiseleva, V. Y. Zaitsev, L. A. Matveev, A. L. Matveyev, S. S. Kuznetsov, E. V. Zagaynova, and N. D. Gladkova, "Optical coherence elastography as a new method for estimation of chemotherapy efficacy on triple-negative breast cancer in the experiment," *Proc. SPIE* **11065**, 1106506 (2019).
22. S. Wang and K. V. Larin, "Optical coherence elastography for tissue characterization: a review," *J. Biophotonics* **8**(4), 279–302 (2015).
23. K. M. Kennedy, L. Chin, R. A. McLaughlin, B. Latham, C. M. Saunders, D. D. Sampson, and B. F. Kennedy, "Quantitative micro-elastography: imaging of tissue elasticity using compression optical coherence elastography," *Sci. Rep.* **5**(1), 15538 (2015).
24. W. M. Allen, L. Chin, P. Wijesinghe, R. W. Kirk, B. Latham, D. D. Sampson, C. M. Saunders, and B. F. Kennedy, "Wide-field optical coherence micro-elastography for intraoperative assessment of human breast cancer margins," *Biomed. Opt. Express* **7**(10), 4139–4153 (2016).
25. K. V. Larin and D. D. Sampson, "Optical coherence elastography - OCT at work in tissue biomechanics [Invited]," *Biomed. Opt. Express* **8**(2), 1172–1202 (2017).
26. E. V. Gubarkova, A. A. Sovetsky, V. Y. Zaitsev, A. L. Matveyev, D. A. Vorontsov, M. A. Sirotkina, L. A. Matveev, A. A. Plekhanov, N. P. Pavlova, S. S. Kuznetsov, A. Y. Vorontsov, E. V. Zagaynova, and N. D. Gladkova, "OCT-elastography-based optical biopsy for breast cancer delineation and express assessment of morphological/molecular subtypes," *Biomed. Opt. Express* **10**(5), 2244–2263 (2019).
27. A. A. Plekhanov, M. A. Sirotkina, A. A. Sovetsky, E. V. Gubarkova, S. S. Kuznetsov, A. L. Matveyev, L. A. Matveev, E. V. Zagaynova, N. D. Gladkova, and V. Y. Zaitsev, "Method for in vivo assessment of cancer tissue inhomogeneity and accurate histology-like morphological segmentation based on Optical Coherence Elastography," *Sci. Rep.* (in press 2020, BioRxiv doi: 10.1101/2020.02.06.937417).
28. A. A. Moiseev, G. V. Gelikonov, D. A. Terpelov, P. A. Shilyagin, and V. M. Gelikonov, "Noniterative method of reconstruction optical coherence tomography images with improved lateral resolution in semitransparent media," *Laser Phys. Lett.* **10**(12), 125601 (2013).
29. V. M. Gelikonov and G. V. Gelikonov, "New approach to cross-polarized optical coherence tomography based on orthogonal arbitrarily polarized modes," *Laser Phys. Lett.* **3**(9), 445–451 (2006).
30. P. A. Shilyagin, L. A. Matveev, E. B. Kiseleva, A. A. Moiseev, V. Y. Zaitsev, A. A. Sovetsky, D. V. Shabanov, V. M. Gelikonov, K. S. Yashin, K. A. Achkasova, N. D. Gladkova, and G. V. Gelikonov, "Stabilization of the Scanning

- Pattern for Three-Dimensional Phase-Sensitive OCT Modalities: Angiography, Relaxography, and Monitoring of Slow Processes,” *Sovrem. Tehnol. Med.* **11**(2), 25–34 (2019).
31. A. Moiseev, L. Snopova, S. Kuznetsov, N. Buyanova, V. Elagin, M. Sirotkina, E. Kiseleva, L. Matveev, V. Zaitsev, F. Feldchtein, E. Zagaynova, V. Gelikonov, N. Gladkova, A. Vitkin, and G. Gelikonov, “Pixel classification method in optical coherence tomography for tumor segmentation and its complementary usage with OCT microangiography,” *J. Biophotonics* **11**(4), e201700072 (2018).
 32. V. Y. Zaitsev, A. L. Matveyev, L. A. Matveev, G. V. Gelikonov, V. M. Gelikonov, and A. Vitkin, “Deformation-induced speckle-pattern evolution and feasibility of correlational speckle tracking in optical coherence elastography,” *J. Biomed. Opt.* **20**(7), 075006 (2015).
 33. V. Y. Zaitsev, A. L. Matveyev, L. A. Matveev, G. V. Gelikonov, E. V. Gubarkova, N. D. Gladkova, and A. Vitkin, “Hybrid method of strain estimation in optical coherence elastography using combined sub-wavelength phase measurements and supra-pixel displacement tracking,” *J. Biophotonics* **9**(5), 499–509 (2016).
 34. A. A. Sovetsky, A. L. Matveyev, L. A. Matveev, D. V. Shabanov, and V. Y. Zaitsev, “Manually-operated compressional optical coherence elastography with effective aperiodic averaging: demonstrations for corneal and cartilaginous tissues,” *Laser Phys. Lett.* **15**(8), 085602 (2018).
 35. A. L. Matveyev, L. A. Matveev, A. A. Sovetsky, G. V. Gelikonov, A. A. Moiseev, and V. Y. Zaitsev, “Vector method for strain estimation in phase-sensitive optical coherence elastography,” *Laser Phys. Lett.* **15**(6), 065603 (2018).
 36. V. Y. Zaitsev, A. L. Matveyev, L. A. Matveev, G. V. Gelikonov, A. A. Sovetsky, and A. Vitkin, “Optimized phase gradient measurements and phase-amplitude interplay in optical coherence elastography,” *J. Biomed. Opt.* **21**(11), 116005 (2016).
 37. V. Y. Zaitsev, A. L. Matveyev, L. A. Matveev, E. V. Gubarkova, A. A. Sovetsky, M. A. Sirotkina, G. V. Gelikonov, E. V. Zagaynova, N. D. Gladkova, and A. Vitkin, “Practical obstacles and their mitigation strategies in compressional optical coherence elastography of biological tissues,” *J. Innovative Opt. Health Sci.* **10**(06), 1742006 (2017).
 38. V. Y. Zaitsev, A. L. Matveyev, L. A. Matveev, G. V. Gelikonov, O. I. Baum, A. I. Omelchenko, D. V. Shabanov, A. A. Sovetsky, A. V. Yuzhakov, A. A. Fedorov, V. I. Siplivy, A. V. Bolshunov, and E. N. Sobol, “Revealing structural modifications in thermomechanical reshaping of collagenous tissues using optical coherence elastography,” *J. Biophotonics* **12**(3), e201800250 (2019).
 39. T. A. Krouskop, T. M. Wheeler, F. Kallel, B. S. Garra, and T. Hall, “Elastic moduli of breast and prostate tissues under compression,” *Ultrason. Imag.* **20**(4), 260–274 (1998).
 40. V. Y. Zaitsev, A. L. Matveyev, L. A. Matveev, E. V. Gubarkova, A. A. Sovetsky, M. A. Sirotkina, G. V. Gelikonov, E. V. Zagaynova, and N. D. Gladkova, and A. Vitkin, *Manifestations of nonlinear elasticity of biological tissues in compressional optical coherence elastography, European Conferences on Biomedical Optics* (SPIE, 2017), Vol. 10413.
 41. A. A. Sovetsky, E. V. Gubarkova, L. A. Matveev, A. L. Matveyev, M. A. Sirotkina, N. D. Gladkova, and V. Y. Zaitsev, *OCT-based characterization of the nonlinear properties of biological tissues in various states*, SPIE Photonics Europe (SPIE, 2018), Vol. 10685.
 42. Y. Wang, L. Dong, Q. Bi, X. Li, D. Wu, X. Ge, X. Zhang, J. Fu, C. Zhang, C. Wang, and S. Li, “Investigation of the efficacy of a bevacizumab-cetuximab-cisplatin regimen in treating head and neck squamous cell carcinoma in mice,” *Target. Oncol.* **5**(4), 237–243 (2010).
 43. S. Mallidi, K. Watanabe, D. Timmerman, D. Schoenfeld, and T. Hasan, “Prediction of tumor recurrence and therapy monitoring using ultrasound-guided photoacoustic imaging,” *Theranostics* **5**(3), 289–301 (2015).
 44. M. M. Tomayko and C. P. Reynolds, “Determination of subcutaneous tumor size in athymic (nude) mice,” *Cancer Chemother. Pharmacol.* **24**(3), 148–154 (1989).
 45. T. Friess, W. Scheuer, and M. Hasmann, “Combination treatment with erlotinib and pertuzumab against human tumor xenografts is superior to monotherapy,” *Clin. Cancer Res.* **11**(14), 5300–5309 (2005).
 46. T. Li, G. Kang, T. Wang, and H. Huang, “Tumor angiogenesis and anti-angiogenic gene therapy for cancer,” *Oncol. Lett.* **16**(1), 687–702 (2018).
 47. B. W. Engbrecht, C. Menon, A. V. Kachur, S. M. Hahn, and D. L. Fraker, “Photofrin-mediated photodynamic therapy induces vascular occlusion and apoptosis in a human sarcoma xenograft model,” *Cancer Res.* **59**(17), 4334–4342 (1999).
 48. E. J. Walker, H. Su, F. Shen, V. Degos, G. Amend, K. Jun, and W. L. Young, “Bevacizumab attenuates VEGF-induced angiogenesis and vascular malformations in the adult mouse brain,” *Stroke* **43**(7), 1925–1930 (2012).
 49. A. X. Zhu, N. S. Holalkere, A. Muzikansky, K. Horgan, and D. V. Sahani, “Early antiangiogenic activity of bevacizumab evaluated by computed tomography perfusion scan in patients with advanced hepatocellular carcinoma,” *Oncologist* **13**(2), 120–125 (2008).